Revisiting the chevrel phase: Impact of dispersion corrections on the properties of Mo_6S_8 for cathode applications

Katharina Helmbrecht,[*,†] Holger Euchner,[*,‡] and Axel Groß[*,†,¶]

†*Institute of Theoretical Chemistry, Ulm University, Albert-Einstein-Allee 11, 89081 Ulm, Germany*

‡*Helmholtz Institute Ulm (HIU) for Electrochemical Energy Storage, Helmholtzstraße 11, 89081 Ulm, Germany*

¶*Helmholtz Institute Ulm (HIU) for Electrochemical Energy Storage, Helmholtzstraße 11, 89081 Ulm, Germany*

E-mail: katharina.helmbrecht@uni-ulm.de; holger.euchner@kit.edu; axel.gross@uni-ulm.de

Abstract

While the Mo_6S_8 chevrel phase is frequently used as cathode material in Mg–ion batteries, theoretical studies on this material are comparatively scarce. The particular structure of the Mo_6S_8 phase, with rather loosely connected cluster entities, points to the important role of dispersion forces in this material. However, so far this aspect has been completely neglected in the discussion of Mo_6S_8 as cathode material for mono– and multivalent–ion batteries. In this work we therefore have studied the impact of dispersion forces on stability and kinetics of Mo_6S_8 intercalation compounds. For this purpose, a series of charge carriers (Li, Na, K, Mg, Ca, Zn, Al) has been investigated. Interestingly, dispersion forces are observed to only slightly affect the lattice spacing of the chevrel phase, nevertheless having a significant impact on insertion voltage and in particular on the charge carrier mobility in the material. Moreover, upon varying the charge carriers in the chevrel phase, their diffusion barriers are observed to scale linearly with the ion size, almost independent of the charge of the considered ions. This indicates a rather unique and geometry dominated diffusion mechanism in the chevrel phase. The consequences of these findings for the ion mobility in the chevrel phase will be carefully discussed.

Introduction

Today, most of the demand for portable energy storage is met by lithium–ion batteries (LIBs), which is largely due to their extraordinary performance, including high energy density, operating voltage and long life cycle.[1,2] However, problems arise in sourcing the needed lithium and cobalt metal,[3] meaning that state of the art LIBs may not be able to fulfill the growing demand for energy storage solutions. Hence, alternative battery concepts and new battery materials are needed which allow for sustainable, safe, compact and high voltage energy storage systemsl.[4,5] While it seems unlikely that alternative battery technologies will be able to surpass Li in the area of portable batteries, there is also a growing demand for

stationary energy storage and heavy-duty systems. The requirements of those can, on the other hand, be met by different battery types. A promising research field with great potential for improvement are multivalent ion batteries, in particular due to their high volumetric capacities as compared to lithium.[6–8] However, of course there are also certain drawbacks: Multivalent batteries suffer from mobility issues due to the higher ionic charge[5,9–12] and also typically exhibit lower operating voltages than LIBs.[7] Additionally, new battery chemistries typically also require the identification and/or development of suitable electrolytes and electrode materials.[5] Being a very abundant metal that can be sourced locally in many countries, makes Mg a promising candidate among the different possibilities for multivalent charge carriers.[13–16] Because of its abundance and low toxicity, it is a viable option for a green and sustainable battery material, moreover offering a high volumetric capacity (3833 $mAh \cdot cm^{-3}$ as compared to 2061 $mAh \cdot cm^{-3}$ in the case of Li). Although there has been increased research interest in Mg batteries, problems with respect to electrolyte stability at the anode and the rather low operating voltage still need to be solved.[5] As a common problem, the insertion of Mg ions on the cathode side is often sluggish and hard to reverse, which is mainly due to the divalent ions being strongly bound at the cathode side.[17]

Multiple cathode materials have been proposed for Mg batteries such as spinels,[18] V_2O_5[19] or the chevrel phase (CP)[13–16] . However, only in the CP the issues of sluggish insertion kinetics and low reversibility are solved more or less satisfactorily.[13–16] The CP was first discovered in 1973 by Chevrel et al. and the corresponding structure is depicted in Fig. 1.[16,20] It consists of an arrangement of Mo_6S_8 clusters, in which a nearly cubic sulfur cage holds an octahedral molybdenum cluster. Sulfur may in principle also be substituted with selenium and tellurium, but as these elements are toxic and therefore can lead to safety problems, we here only concentrate on the sulfur phase. Upon intercalation of divalent Mg, the CP undergoes a two-step charge redistribution process, which is particularly fast, as X-ray photoemission spectroscopy experiments have revealed.[21] The first electron is taken up by the sulfur cage, while the second one then gets transferred on the Mo-cluster. The CP cluster

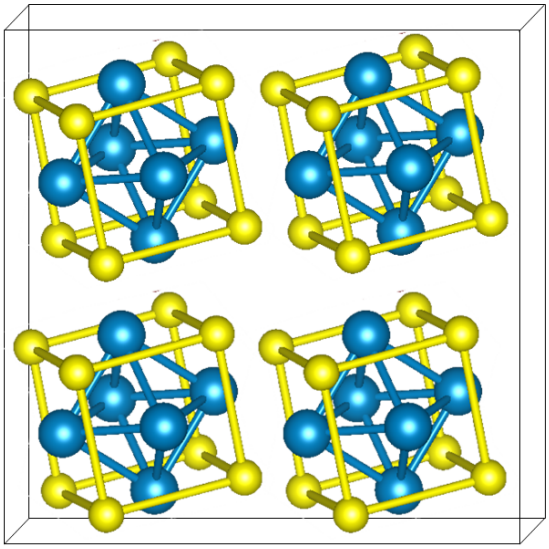

Figure 1: Crystal structure of the chevrel phase (CP). The unit cell consists of one Mo_6S_8 cluster. The units are then stacked in a cubic fashion leaving open channels for diffusion between them. Mo and S atoms are depicted in blue and yellow, respectively.

units are separated by channels, which the ions can intercalate into while causing minimal structural changes, thus allowing for good reversibility. The CP was shown by Aurbach et al. to achieve a discharge voltage between 1 and 1.3 V, with a theoretical energy density of about 135 $Wh \cdot kg^{-1}$.[13–15] From the observed plateaus in the charge/discharge curve, Aurbach et al. also implied the existence of two different insertion sites. After inserting two Mg ions (and their corresponding electrons) into the CP, its valence band is filled and the structure transforms from a metal-like material to a semiconductor.[22]

Possible electrolytes for a Mg ion battery with a CP cathode and Mg metal anode have to be free of oxidizing agents such as water. These are known to passivate the anode in the first cycle and thus are responsible for a quick performance decay.[13] Some commonly used electrolytes are the dichloro complex (DCC),[13] the all-phenyl complex (APC)[23] and the magnesium aluminium chloride complex (MACC).[24] They all contain halide anions as well as organic solvent molecules for stability. The large organic parts of these molecules together with the cluster structure of the CP raise the question about the impact of dispersion interactions at the solid electrolyte interphase (SEI) and also in the CP itself, as dispersion contributes significantly to the interaction of such large organic molecules with surfaces and

materials.[25] However, to the best of our knowledge, dispersion forces have not yet been studied with respect to their effects on the CPs bulk and surface properties. Therefore, we here investigate the bulk diffusion properties as well as adsorption and intercalation processes of various cations in the CP to analyse the impact of the dispersion correction. For this purpose, we, moreover, seek comparison to results obtained without dispersion correction. Finally, the influence of ion size and charge of the intercalated ions on the diffusion properties is discussed.

Computational details

The bulk and surface properties of the CP as well as the ion migration of Mg, Ca, Li, Zn, Na, K and Al inside the phase were studied using periodic density functional theory,[26,27] as implemented in the Vienna *Ab initio* Simulation Package.[28–30] To account for exchange and correlation in the non-dispersion corrected reference systems, the generalized gradient approximation in the formulation of Perdew, Burke and Ernzerhof (PBE)[31] was used. The revised PBE functional (RPBE)[32] in combination with the the Grimme D3 correction with Becke-Johnson damping[33] was applied to account for dispersion effects, as suggested in literature,[34,35] whereas RPBE calculations without dispersion correction were also conducted for comparison. The electron-core interactions are represented by the Projector Augmented Wave (PAW)[36] method. Calculations were first performed for the Mo_6S_8 unit cell of the CP with the Brillouin zone sampled using a 4×4×4 k-point grid. For adsorption, intercalation and ion diffusion, different supercells, which are specified in the respective sections, were used and the k-point grid was scaled accordingly in each lattice direction. The electronic structure was converged to 1×10^{-5} eV, applying a plane-wave cutoff energy of 450 eV. The migration barriers for intercalation and bulk diffusion were obtained by applying the climbing image Nudged Elastic Band (NEB) method.[37] Most NEB calculations were performed using three distinct images along the pathway with a few requiring additional images, while all forces

on the atoms were converged within 0.05 eV $Å^{-1}$.

Results and Discussion

Bulk properties

First, the bulk properties of the CP were determined by using the PBE functional, the RPBE functional and the RPBE+D3 scheme. The resulting lattice parameters are given in table 1 and show that the inclusion of dispersion effects yields a somewhat more densely packed structure, while the lattice geometry remains essentially unchanged. A comparison with an experimentally determined lattice constant shows that the dispersion corrected cell yields a smaller value than the experiment, whereas without accounting for dispersion effects the observed values are both slightly too large.

To evaluate the stability of the CP, the bulk formation energies, E_f, for both approaches were calculated (see table 1) by using the following expression:

$$E_f = \frac{E_{Mo_6S_8} - 6 * E_{Mo} - 8 * E_S}{14} \tag{1}$$

Here, $E_{Mo_6S_8}$ represents the total energy of the optimized Mo_6S_8 phase, whereas E_{Mo} and E_S correspond to the total energies of Mo metal (bcc) and bulk sulfur (S_8). Note that the bulk phase of a metal, such as Mo, should be calculated without applying dispersion corrections. As expected, the dispersion corrected calculation shows a slightly more negative bulk formation energy, which may be understood as a consequence of the stronger inter-cluster interactions, while PBE and RPBE yield a nearly identical energy. Still, the RPBE interaction energy is slightly smaller than the PBE interaction energy, as known for many other systems.[32,38]

In Fig. 2, the total energies of the three different exchange–correlation schemes are depicted as a function of the lattice parameter. Both PBE and RPBE show a qualitatively al-

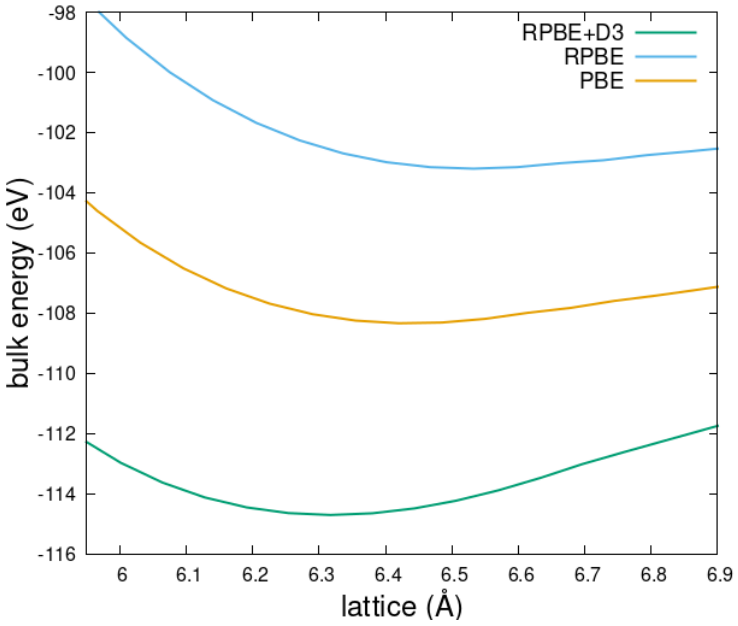

Figure 2: System energy of the bulk in relation to the lattice constant.

most identical behavior with a small slope towards larger lattice parameters. The RPBE+D3 system, on the other hand, shows a stronger increasing energy towards larger lattice parameters. In the following, we are typically comparing results within the RPBE+D3 setup to calculations using PBE as standard reference setup.

Surfaces

As the next step, the (100), (110) and (111) surfaces of the CP were examined. At this point it has to be noticed that the surface terminations of the CP are most stable if all clusters are kept intact. Surfaces calculations with broken clusters, even if nominally smoother than

Table 1: Lattice constants and bulk formation energies for bulk Mo_6S_8 as obtained by using three different exchange–correlation functionals.

	RPBE+D3	RPBE	PBE	exp[39]
lattice (Å)	6.32	6.53	6.48	6.43
Δ to exp	-0.11	0.10	0.05	
angle (°)	91	91	91	91
E_f (eV/at)	-1.26	-1.09	-1.10	/

the surfaces with complete clusters, are associated with significantly higher surface energies. Hence here we only report surface energies for CP surfaces with intact Mo_6S_8 clusters. Each surface was modeled by three cluster layers with the top and bottom layer being relaxed, while a vacuum of 20 Å was placed between them.

The surface energies for the investigated surfaces were calculated following Eqn. 2:

$$E_{surf} = \frac{E_{slab} - nE_{Mo_6S_8}}{2 * A} \tag{2}$$

Here, E_{slab} and $E_{Mo_6S_8}$ represent the total energy of the slab and the bulk phase, whereas A corresponds to the surface area.

The surface energies that were obtained for the dispersion corrected case are in qualitative agreement with the calculations excluding dispersion effects, as can be seen in Tab. 2. Specifically, in both cases the (100) surface was observed to be the most stable one and was thus chosen for all further surface studies. Interestingly, the surfaces were found to be more stable without including dispersion forces in the calculation. This fact can be understood as a consequence of the higher cohesive energies upon including dispersion corrections so that the creation of surfaces by cleaving the CP crystal becomes energetically more costly.

To evaluate the contributions of the different surfaces with respect to the shape of crystallites, a Wulff plot using the surfaces energies was determined,[41] as illustrated in Fig. 3. It is evident that the (100) surface dominates the crystal shape. In fact, for the dispersion corrected system it accounts for 78 % of the total surface area, while in the PBE case it even amounts to 92 %.

Table 2: Surfaces energies calculated with the different functionals (in meV/Å^2).

	RPBE+D3	PBE[40]
(100)	60	24
(110)	78	33
(111)	130	42

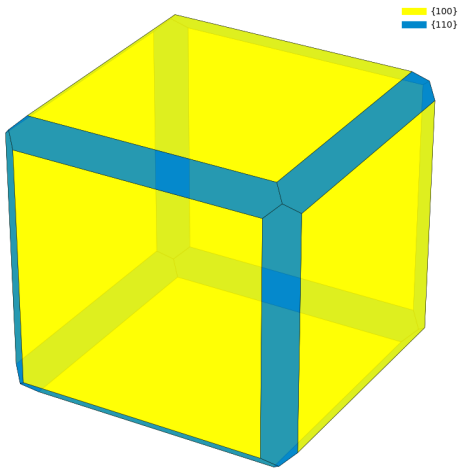

Figure 3: Wulff plot for the surface energies in the CP, with the (100) termination colored in yellow accounting for 78 % of the total surface area in the dispersion corrected system.

Intercalation

To this day, the only cation that is commonly used in experimental setups with the CP is Mg. To allow for direct comparison with earlier studies,[40] the intercalation process for Mg into the CP was analysed, using an adsorbed $MgCl^+$ molecule as starting point for the diffusion process. In fact, previous studies[40] did not take dispersion forces into account and observed a two-step intercalation process, with the first step corresponding to the bond breaking between Mg and Cl with a barrier of 0.2 eV, whereas the second step showed a bulk like diffusion with a barrier of about 0.4 eV. Thus, the overall barrier of the full process amounted to about 0.5 eV. In our study, only one intercalation step is observed, for which the diffusing Mg ion has to overcome a barrier of 0.34 eV to enter into the CP (see Fig. 4). As expected, the endpoint of the diffusion path is energetically more stable than the starting point, proving that the intercalation is indeed favorable. Note that the intercalation barrier determined in this study is much smaller than the one in previous works and points to a more favorable intercalation process. The observed difference is a direct consequence of the dispersion interaction, as the first step of the above described process is obsolete in the dispersion corrected calculations. This is due to the fact that the adsorbed state lies already deeper in the surface with the Mg–Cl bond being already broken.

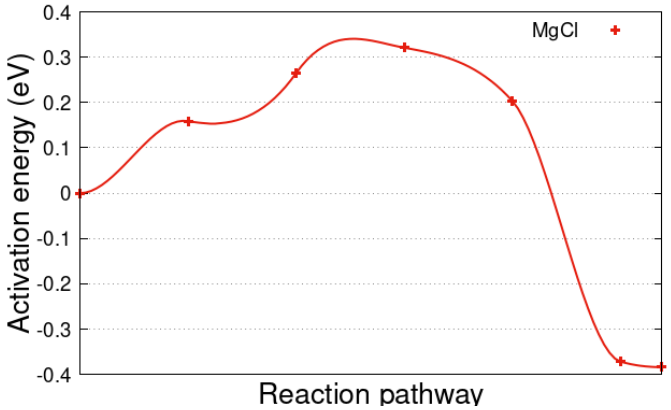

Figure 4: RPBE-D3 derived potential energy curve of the intercalation pathway of Mg (stemming from an adsorbed MgCl) into the (100) CP surface.

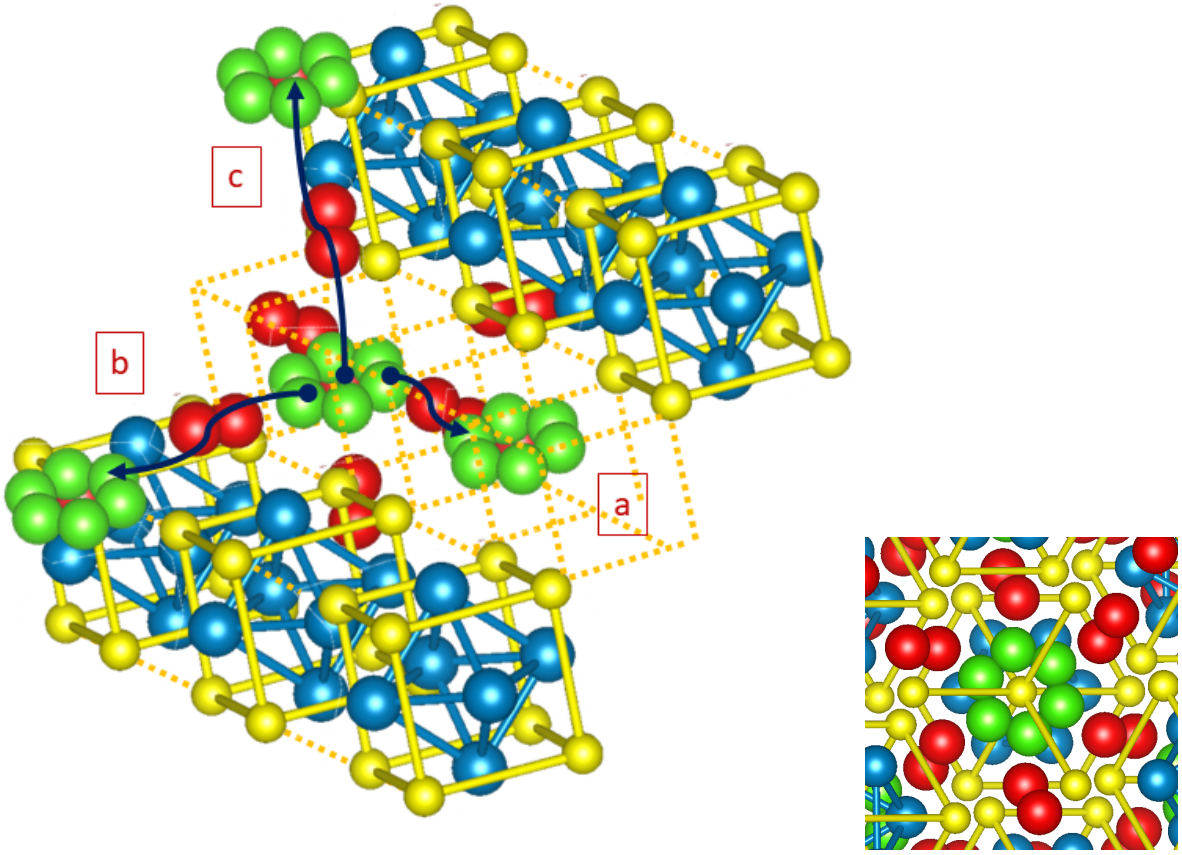

(a) (b)

Figure 5: (a) Visual representation of the diffusion pathways a, b and c. Each leads from one inner ring position (green) inside a cavity over the outer ring positions (red) into the neighboring cavity with the next inner ring position. (b) View along the c-lattice direction showing the arrangement of the inner (green) and outer (red) ring positions.

After elaborating on the differences in the kinetics of the insertion process, the specific mechanism of Mg intercalation into Mo_6S_8 will now further be discussed. From literature [42] it is well-known that two different sites are available for Mg intercalation, the so-called inner and outer ring positions. The inner ring positions are coordinated with eight sulfur atoms, each being the corner of one CP cluster, with altogether 6 possible positions on each inner ring, shown as green spheres in Fig. 5. These positions are nearly degenerate, separated by a barrier of $\approx$0.1 eV .[42] The outer ring positions lie in the channels formed by four cluster edges around the inner ring and have two possible sites per channel with altogether six channels surrounding the inner ring (red spheres in Fig. 5). These outer ring sites are also expected to be degenerate. In agreement with earlier studies, our dispersion corrected calculations find an inner ring position to be the most stable site for the insertion of the first Mg ion, with the six possible positions being essentially energetically equivalent. This was confirmed by placing the Mg cation in all available inner and outer ring positions and comparing the corresponding system energies. As for our previous results, here we also seek comparison to our calculations that are based on the PBE setup. Interestingly, these yield the same energetics for inner and outer ring positions. However, the outer ring sites are found to be only 0.19 eV less stable than the inner ring sites, whereas for the RPBE+D3 approach the difference amounts to 0.56 eV, thus indicating significant differences for the Mg diffusion. For the second intercalated Mg ion, again all different possibilities were evaluated, now finding an outer ring position to be the most favorable site, as the inner ring is too crowded with two occupied sites. With one Mg already sitting on a inner ring site, the outer ring site which is furthest away from this site is found to be the most stable one for the second Mg. This results in more and less stable combinations of inner and outer ring sites. For the determination of the voltages, we always chose the most stable combination in which there was the maximum possible distance between the ions. To allow for direct comparison to earlier studies as well as to experimental data, the corresponding insertion voltages with respect to the corresponding metal anodes have been determined for each intercalation step,

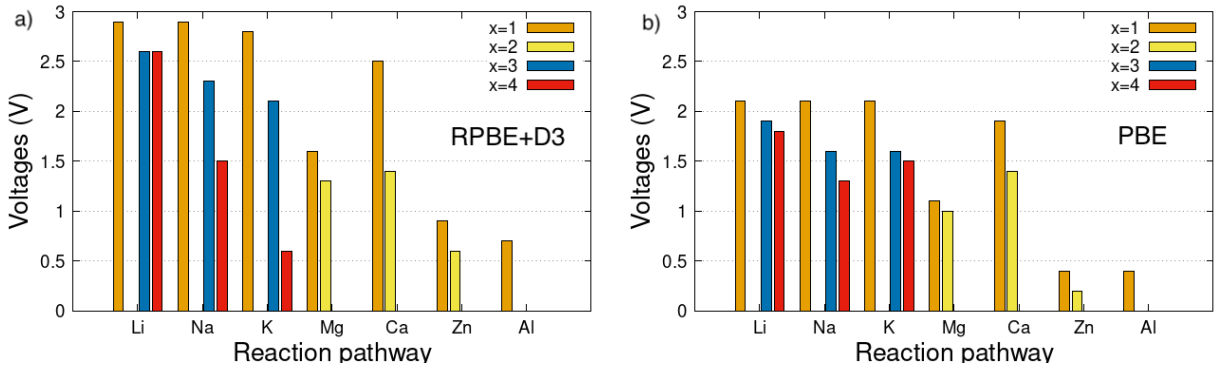

Figure 6: Calculated insertion voltages (in V) for a variety of different metal ions M^{n+} as a function of the metal loading x for $M_xMo_6S_8$, determined using Eq. 3 and a) the RPBE+D3 functional, b) the PBE functional.

according to

$$V_{\mathrm{M},x} = -\frac{E_{\mathrm{M}_x\mathrm{Mo_6S_8}} - E_{\mathrm{M}_{x-1}\mathrm{Mo_6S_8}} - E_{\mathrm{M}}}{z_{\mathrm{M}}} \tag{3}$$

Here, $E_{E_{\mathrm{M}_x\mathrm{Mo_6S_8}}}$ is the energy of the CP system containing x atoms of metal M per Mo_6S_8 formular unit, whereas $E_{\mathrm{M}_{x-1}\mathrm{Mo_6S_8}}$ corresponds to the energy of the system holding $x-1$ metal atoms. E_{M} is the bulk energy per atom for the respective metal and z_{M} is the specific charge of the metals cation. Note that this insertion voltage corresponds to the open circuit voltage when the corresponding metal is used as the anode.[43,44]

The resulting voltages for the first two ionic intercalation steps of Mg are shown in Fig. 6a, amounting to ∼1.6 and ∼1.3 V, respectively, using the RPBE+D3 functional. This is in decent agreement with the experimental values of 1.0–1.3 V.[13] For comparison, the Mg insertion voltages were also determined without dispersion correction (see Fig. 6b). For the PBE reference, slightly lower values of ∼1.1 and 1.0 V have been obtained, indicating a smaller voltage difference between the insertion of the first and the second Mg atom. Additionally, the voltages were calculated for the RPBE functional without considering dispersion effects (not shown in Fig. 6). This resulted in voltages of 0.9 and 0.8 V for the two intercalation steps, *i.e.*, slightly smaller values than calculated with PBE.

As a next step, Li, Na, K, Ca, Zn and Al intercalation was also considered with and without dispersion corrections to derive chemical trends and further elucidate the effect of

dispersion corrections. To identify the most stable intercalation sites, all possible configurations for the insertion of the different charge carriers were again investigated in the previously specified way. Note that the maximum number of inserted charge carriers is chosen with respect to their formal charge, thus meaning the insertion of up to four monovalent, two divalent and one trivalent charge carrier. As expected, the most stable intercalation sites were observed to be the same for all metals, with the first cation filling one of the inner ring positions, and the others consecutively filling up the outer ring positions in each lattice direction while for the second and third keeping a maximum distance to the atom on the inner ring.

For all divalent ions, the same configurations as for Mg have been observed to be the most stable ones and were evaluated to determine the corresponding insertion voltages (see Fig. 6). In the case of Ca a voltage increase as compared to the insertion of Mg is observed, which is more pronounced in the dispersion corrected systems for both insertion steps. The calculations of Juran et al.[45] reach a voltage of 2.1 and 1.8 V for the respective intercalation steps of Ca using the HSE functional which agree reasonably well with our values of 2.5 and 1.4 V for the dispersion corrected systems, as well as 1.9 and 1.4 V for the uncorrected PBE reference calculation. Zn, on the other hand, shows voltages below 1 V, again with slightly higher values for the dispersion corrected case. For Zn, there is an experimentally reported voltage of 0.3-1.0 V[46] into which the dispersion corrected values of 0.9 and 0.6 V fit well, while the non-corrected PBE results of 0.2 and 0.4 V obviously underestimate the intercalation energies. Al shows a similar behavior with values of 0.7 V (RPBE+D3) and 0.4 V (PBE) for the intercalation of one Al ion, again agreeing rather well with the experimentally reported value of 0.5 V.[47] Formally only 1.3 Al ions can be intercalated per unit cell (4 electrons limit per CP unit), which is confirmed by the fact that the intercalation of a second Al into the CP is found to be energetically unfavorable.

For the monovalent ions, the above described most stable arrangements were investigated. Interestingly enough, the intercalation of the second monovalent ion is found to be unstable,

which is also supported by previous experimental studies that show a voltage plateau between x=1 and x=3.[7] A possible reason for this might be that the distortion due to one filled outer ring position is energetically more expensive as distortions in two or three lattice directions.

Therefore, insertion voltages have only been evaluated for the stable configurations (*i.e.*, with x=1, x=3 and x=4) of the monovalent metals Li, Na and K, again using Eq. 3. The first intercalation step for Li, Na and K shows significantly increased voltages as compared to the multivalent ions (see Fig. 6). Moreover, the dispersion corrected RPBE+D3 calculations again yield a larger voltage (over 2.5 V for all monovalent metals) as the PBE case (the first step results in a voltage of about 2.1 V for all monovalent metals). Furthermore, with increasing cation concentration the voltage is decreasing, with a more drastic decrease for the larger cations.

Ion mobility

While the surface properties determine the kinetics of the insertion into the electrode, the cation diffusion through a material is determined by its bulk properties. The diffusion barriers for charge carrier migration inside the bulk CP are also of great interest[10,11] and were therefore determined for the above discussed series of charge carriers (Mg, Ca, Li, Na, K, Zn and Al). The comparison of the different metals allows the investigation of the factors that determine the diffusion kinetics in the CP.

Before extending the study to all investigated charge carriers, the case of Mg will be discussed in detail. As elaborated above, the most stable position for one Mg ion in the CP bulk phase is an inner ring position. From there it can diffuse in the three lattice directions a, b and c by passing over two outer ring positions to the next inner ring site.[48] The different spatial diffusion pathways are depicted in Fig. 5 and it can be seen that the c pathway is the same for all combinations of start and end site on the inner ring, because the inner ring is perpendicular to the diffusion pathway.

This is not the case for pathways a and b as some of their inner ring positions lie near the

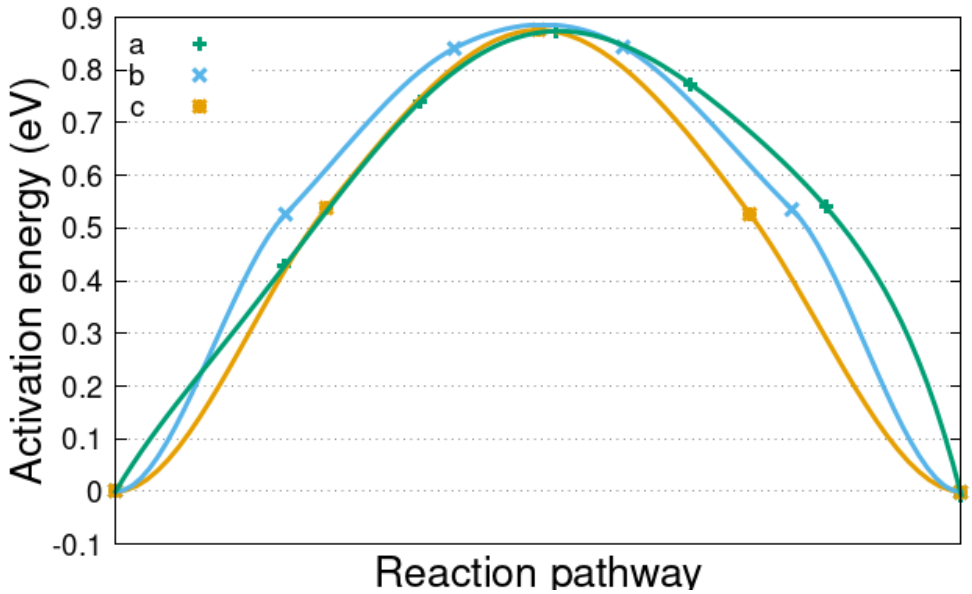

Figure 7: Barriers for Mg diffusion along the a, b and c pathways determined with the RPBE+D3 functional.The lines serve as a visual guide.

edge of the transition cavity and the whole inner ring is parallel to the diffusion direction. Here, depending on the initial site, the Mg might diffuse directly or via a neighboring inner ring site, resulting in a few different possible diffusion pathways. For our calculations we thus placed the Mg in the inner ring position closest to the transition cavity for the pathways a and b as to exclude inner ring diffusion from the pathway. After extrapolation all three pathways showed a barrier of about 0.88 eV (see Fig. 7), which is due to the fact that the transition state for the different pathways is almost identical.

The transition state for all diffusion paths lies between the two outer ring positions in a transition cavity. This bottleneck is formed by the place in which the cation has to pass two opposite sulfur corners of the CP cluster and is characterized by the distance between the diffusing cation and these sulfur atoms. For pathway a and b the distances to the first sulfur atom amount to 2.32, while the second one is slightly further apart (2.35 Å). Hence, the cation is shifted away from the central position, which is a consequence of the asymmetric path. For the c pathway, the distance to both sulfur atoms corresponds to 2.30 Å, which then leads to the symmetrical transition state.

To elaborate on the direct consequences of the dispersion correction, the Mg migration pathways have also been calculated utilizing the PBE functional – *i.e.*, without accounting for dispersion effects. Their heights were 0.31 and 0.38 eV for a/b and c respectively. Note that earlier PBE studies found diffusion barriers of 0.5 eV,[22] 0.27 eV[49] and 0.51 eV.[50] All these barrier heights are significantly smaller than those obtained using the RPBE+D3 functional. At first sight, this does not seem to be too surprising considered the fact that also the PBE intercalation energies are considerably smaller than those determined with the RPBE+D3 functional which indicates that PBE yields a weaker interaction and thus also smaller barrier heights.

However, one also has to take into account that these two different functionals produce different lattice constants for the CP phase. The distance to the sulfur atoms in the PBE calculation amount to 2.38 and 2.41 Å for pathway a and b, while 2.35 Å are obtained for both distances in pathway c. This leads to an about 0.05 Å larger Mg–S separation compared to the dispersion corrected cases. Although this seems to be a rather small change, one has to consider that the decrease in the lattice spacing might more significantly influence the energetics in the bottleneck of the diffusion pathway between the two sulfur atoms which the cations have to pass at the transition state of a diffusion process.

In order to check whether indeed this narrowing has an effect on the diffusion barriers, dispersion corrected NEB calculations were performed on the PBE optimized structure. If the increased barriers were mainly due to specific dispersion interactions one would also expect increased barriers for this scenario. On the other hand, NEB calculations using the PBE functional without dispersion corrections were conducted on the RPBE+D3 optimized structure. Indeed, in the first case, a barrier of 0.43 eV was observed, which is only slightly higher than the corresponding PBE calculated barrier of 0.31 eV. For the second case, the barrier amounted to 0.80 eV and was thus almost as high as the 0.88 eV obtained in the RPBE+D3 calculation. This comparison convincingly highlights that it is indeed the geometry of the CP, particular the distance between the Mo_6S_8 clusters and thus the size of

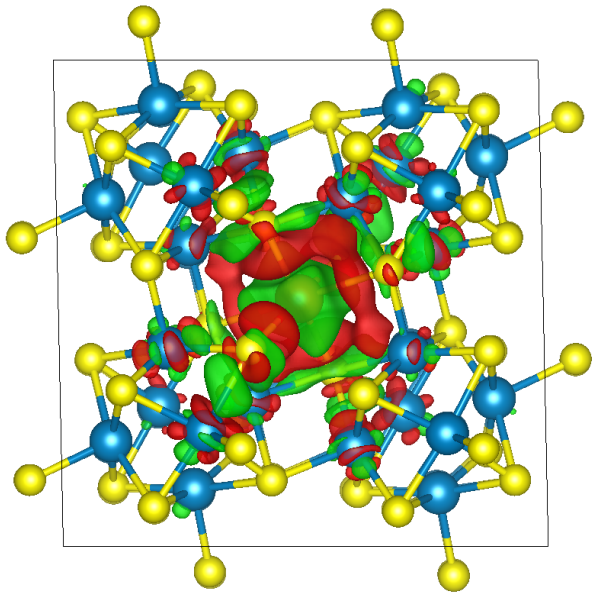

Figure 8: Charge density difference plot of the transition state calculated with RPBE+D3. Accumulation of charge is shown in red and depletion in green.

the bottleneck, which determines the height of the barriers. Consequently, already small differences in lattice constant may have a quite significant impact. This can be understood based on the notion that the increase in the potential energy close to the transition state is mainly mediated by Pauli repulsion which is exponentially increasing upon lowering the distances. This would then explain the sensitive dependence of the diffusion barrier on the lattice spacing.

To complete this discussion, the diffusion path was also determined with the RPBE functional, yielding a barrier of 0.55 eV, *i.e.*, somewhat higher as for the PBE scenario. On the other hand, when using the RPBE setup for a NEB calculation based on the PBE and RPBE+D3 geometry, barriers of 0.47 and 0.81 were obtained, respectively. This agrees well with the above discussed results, again pointing to the fact that the available space at the transition state configuration is the most important factor influencing the barrier height. It has to be emphasized that these findings show the importance of the dispersion forces for the atomic distances in the CP phase, whereas the difference in barrier height is neither directly the result of an enhanced dispersion interaction at the transition state, nor a straight

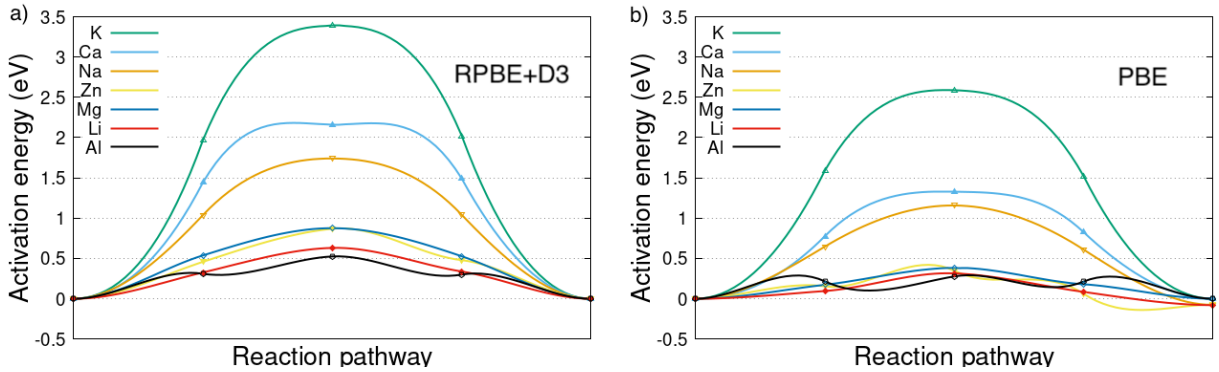

Figure 9: Minimum energy pathways for the investigated charge carriers along pathway c, calculated with the RPBE+D3 setup (a) and with the pure PBE functional (b).

consequence of the particular exchange-correlation functional.

For gaining further understanding of the transition state, charge density difference plots have been determined. In Fig. 8 we can see that most of the charge density difference is located on the sulfur cage edges closest to the diffusing Mg. The shape of the charge distribution is qualitatively very similar for the three investigated functionals, therefore only the RPBE+D3 results are depicted. It can be observed that the distorted cube shape of the chevrel clusters is mirrored in the distorted cube shape of the charge density difference, while charge accumulation is visible on the sulfur edge atoms (red). These atoms form the before mentioned bottleneck and this charge accumulation together with the corresponding Mg–S distances may thus be understood as the decisive factor for the transition state energy and hence the barrier.

Finally, in order to investigate the chemical trends in the diffusion behavior for various charge carriers, the bulk migration barriers for the previously discussed charge carriers were determined and compared. Due to its symmetry, pathway c was selected for these NEB calculations. Again, to allow for comparison the corresponding barriers were calculated using both the RPBE+D3 and the PBE functional and all resulting minimum energy pathways are depicted in Figs. 9a and b. As in the case of Mg, the NEB results show a distinct maximum in the middle of the pathway: *i.e.*, for the bottleneck of the charge carrier diffusion. For all charge carriers, the barriers calculated with the PBE functional are lower than their

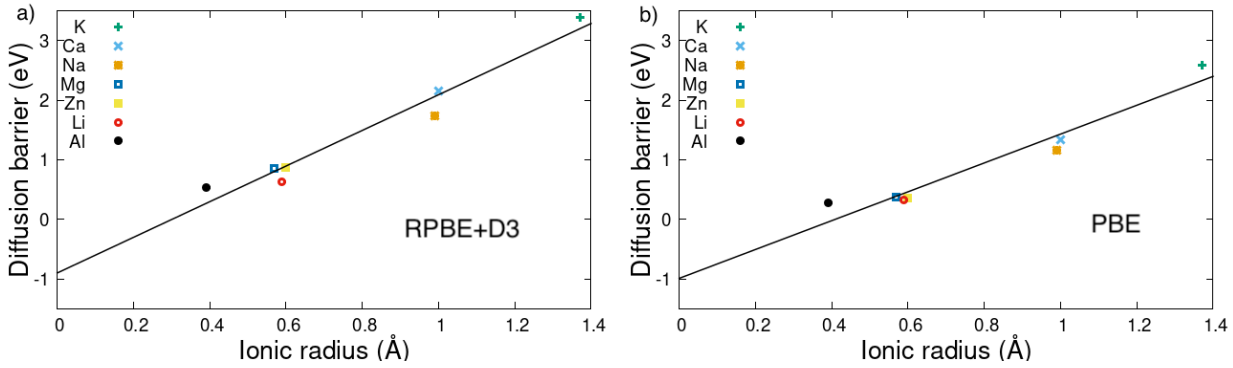

Figure 10: Correlation between ionic radius (in Å) and the diffusion barrier of pathway c (in eV) for various charge carriers, determined using the RPBE+D3 functional (a) and the PBE functional (b).

RPBE+D3 counterparts, again, pointing to geometric constraints as the determining factor for the barrier height.

Interestingly, a closer investigation of the obtained diffusion barriers for the different metals in the CP shows a direct correlation between the ionic radius and the diffusion barrier of the charge carrier. As can be seen from Fig. 10, this linear correlation is well fulfilled for both RPBE+D3 and PBE calculations. There are still slight discrepancies from a perfect scaling. The monovalent Li ion has a sightly smaller barrier than the divalent Mg and Zn ions, while they all exhibit a similar ionic radius, hence a smaller charge leads to a slightly smaller diffusion barrier. Still, it can be concluded that the ionic radius is indeed the most important factor for the charge carrier diffusion in the CP. This strong dependence of the diffusion barriers on the ion size of the charge carriers confirms that the chevrel phase exhibits unique characteristics, as far as the ion mobility is concerned. Our calculations provide strong evidence that this ion mobility is governed by geometric restrictions, *i.e.*, by the available space at the transition state for diffusion. It is important to realize that ion mobility in the chevrel phase, which consists of an assembly of large, relatively inert building blocks, is governed by factors that are different from those that are critical for, say, oxides and sulfides in the spinel structure[10,12] .

Furthermore, as it is very likely that dispersion contributes to the interaction between the

Mo_6S_8 clusters in the chevrel phase, previous calculations may have overestimated the lattice spacing in the chevrel phase by not taking the dispersion interaction into account and thus underestimated the height of the diffusion barriers. Consequently, our findings indicate that the ion mobility in the chevrel phase might be lower than suggested from previous electronic structure calculations.

Conclusions and Summary

The properties of the Mo_6S_8 chevrel phase as a cathode material for Mg ion batteries have been revisited based on density functional theory calculations, in particular considering dispersion corrections. Experimentally determined Mg insertion voltages are satisfactorily reproduced, including dispersion corrections in the exchange-correlation functional,. The additional attractive dispersion interaction leads to a small contraction of the lattice constant of the chevrel phase which, however, has a significant impact on the height of the diffusion barriers of charge carriers in the chevrel phase. Using different computational setups with and without dispersion corrections we have shown that the increase in the diffusion barrier height is not directly mediated by the additional attractive dispersion interactions, but rather by space limitations at the transition state for diffusion. This notion is further supported by our findings that the diffusion barrier heights scale linearly with the size of the migrating ions, almost independent of their charge. This predominant size dependence of the ion diffusion barrier appears to be a unique feature of the chevrel phase. Furthermore, our findings suggest that previous computational studies that did not take dispersion interaction into account underestimated the ion diffusion barriers in the chevrel phase and thus overestimated the ion mobility in this material.

Acknowledgments

Financial support by the Deutsche Forschungsgemeinschaft (DFG, German Research Foundation) under Germany´s Excellence Strategy – EXC 2154 – Project number 390874152 (POLiS Cluster of Excellence) is gratefully acknowledged. Computer time was provided by the state of Baden-Württemberg through bwHPC and the German Research Foundation (DFG) through grant no INST 40/575-1 FUGG (JUSTUS 2 cluster). This work contributes to the research performed at CELEST (Center for Electrochemical Energy Storage Ulm-Karlsruhe)

References

(1) Goodenough, J. B.; Park, K.-S. The Li-Ion Rechargeable Battery: A Perspective. *J. Am. Chem. Soc.* **2013**, *135*, 1167–1176.

(2) Larcher, D.; Tarascon, J.-M. Towards greener and more sustainable batteries for electrical energy storage. *Nat. Chem.* **2015**, *7*, 19–29.

(3) Vaalma, C.; Buchholz, D.; Weil, M.; Passerini, S. A cost and resource analysis of sodium-ion batteries. *Nat. Rev. Mat.* **2018**, *3*, 18013.

(4) Vinayan, B. P.; Euchner, H.; Zhao-Karger, Z.; Cambaz, M. A.; Li, Z.; Diemant, T.; Behm, R. J.; Groß, A.; Fichtner, M. Insights into the electrochemical processes of rechargeable magnesium–sulfur batteries with a new cathode design. *J. Mater. Chem. A* **2019**, *7*, 25490–25502.

(5) Maroni, F.; Dongmo, S.; Gauckler, C.; Marinaro, M.; Wohlfahrt-Mehrens, M. Through the Maze of Multivalent-Ion Batteries: A Critical Review on the Status of the Research on Cathode Materials for Mg^{2+} and Ca^{2+} Ions Insertion. *Batteries Supercaps* **2021**, *4*, 1221–1251.

(6) Mao, M.; Gao, T.; Hou, S.; Wang, C. A critical review of cathodes for rechargeable Mg batteries. *Chem. Soc. Rev.* **2018**, *47*, 8804–8841.

(7) Rogosic, J. Towards the development of calcium ion batteries. type, PhD Tesis at: Massachusetts Institute of Technology, Department of Materials Science and Engineering,.

(8) Li, Z.; Vinayan, B. P.; Jankowski, P.; Njel, C.; Roy, A.; Vegge, T.; Maibach, J.; Lastra, J. M. G.; Fichtner, M.; Zhao-Karger, Z. Multi-Electron Reactions Enabled by Anion-Based Redox Chemistry for High-Energy Multivalent Rechargeable Batteries. *Angew. Chem. Int. Ed.* **2020**, *59*, 11483–11490.

(9) R.V.Noorden, The rechargeable revolution: A better battery. *Nature* **2014**, *504*, 26–28.

(10) Bachman, J. C.; Muy, S.; Grimaud, A.; Chang, H.-H.; Pour, N.; Lux, S. F.; Paschos, O.; Maglia, F.; Lupart, S.; Lamp, P. et al. Inorganic Solid-State Electrolytes for Lithium Batteries: Mechanisms and Properties Governing Ion Conduction. *Chem. Rev.* **2016**, *116*, 140–162.

(11) Dillenz, M.; Sotoudeh, M.; Euchner, H.; Groß, A. Screening of Charge Carrier Migration in the $MgSc_2Se_4$ Spinel Structure. *Front. Energy Res.* **2020**, *8*, 584654.

(12) Sotoudeh, M.; Dillenz, M.; Groß, A. Mechanism of Magnesium Transport in Spinel Chalcogenides. *Adv. Energy Sustainability Res.* **2021**, *2*, 2100113.

(13) Aurbach, D.; Lu, Z.; Schechter, A.; Gofer, Y.; Gizbar, H.; Turgeman, R.; Cohen, Y.; Moshkovich, M.; Levi, E. Prototype systems for rechargeable magnesium batteries. *Nature* **2000**, *407*, 724–727.

(14) Mitelman, A.; Levi, M. D.; Lancry, E.; Levi, E.; Aurbach, D. New cathode materials for rechargeable Mg batteries: fast Mg ion transport and reversible copper extrusion in $Cu_yMo_6S_8$ compounds. *Chem. Commun.* **2007**, 4212–4214.

(15) Yoo, H. D.; Shterenberg, I.; Gofer, Y.; Gershinsky, G.; Pour, N.; Aurbach, D. Mg rechargeable batteries: an on-going challenge. *Energy Environ. Sci.* **2013**, *6*, 2265–2279.

(16) Levi, E.; Lancry, E.; Mitelman, A.; Aurbach, D.; Ceder, G.; Morgan, D.; Isnard, O. Phase Diagram of Mg Insertion into Chevrel Phases, $Mg_xMo_6T_8$ (T = S, Se). 1. Crystal Structure of the Sulfides. *Chem. Mater.* **2006**, *18*, 5492–5503.

(17) Canepa, P.; Sai Gautam, G.; Hannah, D. C.; Malik, R.; Liu, M.; Gallagher, K. G.; Persson, K. A.; Ceder, G. Odyssey of Multivalent Cathode Materials: Open Questions and Future Challenges. *Chem. Rev.* **2017**, *117*, 4287–4341.

(18) Liu, M.; Rong, Z.; Malik, R.; Canepa, P.; Jain, A.; Ceder, G.; Persson, K. A. Spinel compounds as multivalent battery cathodes: a systematic evaluation based on ab initio calculations. *Energy Environ. Sci.* **2015**, *8*, 964–974.

(19) Fu, Q.; Sarapulova, A.; Trouillet, V.; Zhu, L.; Fauth, F.; Mangold, S.; Welter, E.; Indris, S.; Knapp, M.; Dsoke, S. et al. In Operando Synchrotron Diffraction and in Operando X-ray Absorption Spectroscopy Investigations of Orthorhombic V_2O_5 Nanowires as Cathode Materials for Mg-Ion Batteries. *J. Am. Chem. Soc.* **2019**, *141*, 2305–2315.

(20) Chevrel, R.; Sergent, M.; Prigent, J. Un nouveau sulfure de molybdene : Mo_3S_4 preparation, proprietes et structure cristalline. *Mater. Res. Bull.* **1974**, *9*, 1487–1498.

(21) Richard, J.; Benayad, A.; Colin, J.-F.; Martinet, S. Charge Transfer Mechanism into the Chevrel Phase Mo_6S_8 during Mg Intercalation. *J. Phys. Chem. C* **2017**, *121*, 17096–17103.

(22) Thöle, F.; Wan, L. F.; Prendergast, D. Re-examining the Chevrel phase Mo_6S_8 cathode for Mg intercalation from an electronic structure perspective. *Phys. Chem. Chem. Phys.* **2015**, *17*, 22548–22551.

(23) Gizbar, H.; Vestfrid, Y.; Chusid, O.; Gofer, Y.; Gottlieb, H. E.; Marks, V.; Aurbach, D. Alkyl Group Transmetalation Reactions in Electrolytic Solutions Studied by Multinuclear NMR. *Organometallics* **2004**, *23*, 3826–3831.

(24) Doe, R. E.; Han, R.; Hwang, J.; Gmitter, A. J.; Shterenberg, I.; Yoo, H. D.; Pour, N.; Aurbach, D. Novel, electrolyte solutions comprising fully inorganic salts with high anodic stability for rechargeable magnesium batteries. *Chem. Commun.* **2014**, *50*, 243–245.

(25) Buchner, F.; Forster-Tonigold, K.; Bozorgchenani, M.; Gross, A.; Behm, R. J. Interaction of a Self-Assembled Ionic Liquid Layer with Graphite(0001): A Combined Experimental and Theoretical Study. *J. Phys. Chem. Lett.* **2016**, *7*, 226–233.

(26) Hohenberg, P.; Kohn, W. Inhomogeneous Electron Gas. *Phys. Rev.* **1964**, *136*, B864–B871.

(27) Kohn, W.; Sham, L. J. Self-Consistent Equations Including Exchange and Correlation Effects. *Phys. Rev.* **1965**, *140*, A1133–A1138.

(28) Kresse, G.; Hafner, J. Ab initio molecular dynamics for liquid metals. *Phys. Rev. B* **1993**, *47*, 558–561.

(29) Kresse, G.; Furthmüller, J. Efficient iterative schemes for ab initio total-energy calculations using a plane-wave basis set. *Phys. Rev. B* **1996**, *54*, 11169–11186.

(30) Kresse, G.; Joubert, D. From ultrasoft pseudopotentials to the projector augmented-wave method. *Phys. Rev. B* **1999**, *59*, 1758–1775.

(31) Perdew, J. P.; Burke, K.; Ernzerhof, M. Generalized Gradient Approximation Made Simple. *Phys. Rev. Lett.* **1996**, *77*, 3865–3868.

(32) Zhang, Y.; Yang, W. Comment on "Generalized Gradient Approximation Made Simple". *Phys. Rev. Lett.* **1998**, *80*, 890–890.

(33) Grimme, S.; Ehrlich, S.; Goerigk, L. Effect of the damping function in dispersion corrected density functional theory. *J. Comput. Chem.* **2011**, *32*, 1456–1465.

(34) Tonigold, K.; Groß, A. Dispersive interactions in water bilayers at metallic surfaces: A comparison of the PBE and RPBE functional including semiempirical dispersion corrections. *J. Comput. Chem.* **2012**, *33*, 695–701.

(35) Mahlberg, D.; Sakong, S.; Forster-Tonigold, K.; Groß, A. Improved DFT Adsorption Energies with Semiempirical Dispersion Corrections. *J. Chem. Theory Comput.* **2019**, *15*, 3250–3259.

(36) Blöchl, P. E. Projector augmented-wave method. *Phys. Rev. B* **1994**, *50*, 17953–17979.

(37) Sheppard, D.; Terrell, R.; Henkelman, G. Optimization methods for finding minimum energy paths. *J. Chem. Phys.* **2008**, *128*, 134106.

(38) Gohda, Y.; Schnur, S.; Groß, A. Influence of water on elementary reaction steps in electrocatalysis. *Faraday Discuss.* **2008**, *140*, 233–244.

(39) Potel, M.; Gougen, P.; Chevrel, R.; Sergent, M. Labilité des cations dans les chalcogénures ternaires de molybdène: voies d'accès à de nouvelles synthèses. *Rev. chim. miner.* **1984**,

(40) Wan, L. F.; Perdue, B. R.; Apblett, C. A.; Prendergast, D. Mg Desolvation and Intercalation Mechanism at the Mo_6S_8 Chevrel Phase Surface. *Chem. Mater.* **2015**, *27*, 5932–5940.

(41) Rahm, J. M.; Erhart, P. WulffPack: A Python package for Wulff constructions. *J. Open Source Softw.* **2020**, *5*, 1944.

(42) Ling, C.; Suto, K. Thermodynamic Origin of Irreversible Magnesium Trapping in Chevrel Phase Mo_6S_8: Importance of Magnesium and Vacancy Ordering. *Chem. Mater.* **2017**, *29*, 3731–3739.

(43) Islam, M. S.; Fisher, C. A. J. Lithium and sodium battery cathode materials: computational insights into voltage, diffusion and nanostructural properties. *Chem. Soc. Rev.* **2014**, *43*, 185–204.

(44) Groß, A. Fundamental Challenges for Modeling Electrochemical Energy Storage Systems at the Atomic Scale. *Top. Curr. Chem.* **2018**, *376*, 17.

(45) Juran, T. R.; Smeu, M. Hybrid density functional theory modeling of Ca, Zn, and Al ion batteries using the Chevrel phase Mo_6S_8 cathode. *Phys. Chem. Chem. Phys.* **2017**, *19*, 20684–20690.

(46) Chae, M. S.; Heo, J. W.; Lim, S.-C.; Hong, S.-T. Electrochemical Zinc-Ion Intercalation Properties and Crystal Structures of $ZnMo_6S_8$ and $Zn_2Mo_6S_8$ Chevrel Phases in Aqueous Electrolytes. *Inorg. Chem.* **2016**, *55*, 3294–3301.

(47) Geng, L.; Lv, G.; Xing, X.; Guo, J. Reversible Electrochemical Intercalation of Aluminum in Mo_6S_8. *Chem. Mater.* **2015**, *27*, 4926–4929.

(48) Levi, E.; Gershinsky, G.; Aurbach, D.; Isnard, O. Crystallography of Chevrel Phases, MMo_6T_8 (M = Cd, Na, Mn, and Zn, T = S, Se) and Their Cation Mobility. *Inorg. Chem.* **2009**, *48*, 8751–8758.

(49) Smeu, M.; Hossain, S.; Wang, Z.; Timoshevskii, V.; Bevan, K.; Zaghib, K. Theoretical investigation of Chevrel phase materials for cathodes accommodating Ca^{2+} ions. *J. Power Sources* **2016**, *306*, 431–436.

(50) Cho, J.-H.; Ha, J. H.; Lee, J. G.; Kim, C.-S.; Cho, B. W.; Kim, K.-B.; Chung, K. Y. Systematic Investigation into Mg^{2+}/Li^{+} Dual-Cation Transport in Chevrel Phases Using Computational and Experimental Approaches. *J. Phys. Chem. C* **2017**, *121*, 12617–12623.